Direct-drive laser target designs for sub-MegaJoule energies

D.G. Colombant,* A.J. Schmitt, S.P. Obenschain, S.T. Zalesak, A.L. Velikovich, and J.W. Bates
Plasma Physics Division, Naval Research Laboratory, Washington, DC, 20375

D.E. Fyfe
LCP&FD, Naval Research Laboratory, Washington, DC, 20375

J.H. Gardner
BRA, Springfield, VA

W. Manheimer
RSI, Lanham, MD, 20706

New direct-drive laser target designs with KrF laser light take advantage of the shorter wavelength to lower the laser energy required for substantial gain (>30x) to sub-MJ level. These low laser-energy pellets are useful in systems that could form an intermediate step towards fusion energy, such as the proposed Fusion Test Facility [S. P. Obenschain,*et al*, Phys. Plasmas **13**, 056320 (2006)]. The short wavelength laser should allow higher intensity (and higher pressure) without increasing the risk of laser-plasma instabilities. The higher pressure in turn allows higher velocities to be achieved while keeping the low aspect ratios required for hydrodynamic stability. The canonical laser energy has been chosen to be 500 kJ. A target design is presented with various laser pulse shapes and both 1D and 2D simulation results are shown. The sensitivity of these targets to both low-mode and high-mode perturbations is examined. The analysis and simulations in this paper indicate that significant gain (G=57) can be achieved for these targets even in the presence of hydrodynamic instabilities.

I. INTRODUCTION

The first proposal for direct-drive laser fusion was published around 35 years ago [1] and has progressed from a visionary concept to a more realistic one. The first target designs were predicted to get 'breakeven' or gains greater than 1 at around 1 kJ of laser energy. Quite rapidly, that number increased to 10's then 100's of kJoules to finally settle at the megaJoule level. For the past 25 years or so, >1 MJ has been considered to be the entry level number for achieving ignition and significant gain. But MJ lasers are huge in size, costly and complex. Reducing this number, even by a moderate factor 2 to 3 is a goal worth pursuing and would represent a major step towards the feasibility of direct-drive laser fusion. However, the need for a gain high enough to overcome the modest laser efficiency has tempered that search for a reduced laser energy. Gain-energy curves [2] show a sharp rise above a given laser energy threshold and conventional wisdom has dictated a laser energy well above that threshold. With advances in laser technology, computational capabilities and 30 years of experiments it is appropriate to revise the assumptions behind the laser energy threshold.

Another factor that has been pivotal in our efforts is the progress in Krypton Fluoride (KrF) laser development at the Naval Research Laboratory (NRL). That laser was first shown to achieve a very high level of illumination uniformity [5] and presents the advantage of a shorter wavelength that had not been taken advantage of fully until very recently. Last year, NRL presented a new path to direct-drive laser fusion and proposed the Fusion Test Facility (FTF) [6]. The goal of this effort is to generate enough fusion power to test substantial components of a fusion power plant. 150 MW is a desirable goal but even 30 MW would be enough for materials testing. These numbers translate into gains of 60-12 @ 5 Hz and a laser energy of around 0.5 MJ. In the past year, we have improved our results (we now have a design with a gain of 57 which appears to be resistant to hydrodynamic instabilities) and we have concentrated on the early-time behavior of the target when the Richtmeyer-Meshkov instability takes place and provides the seeds for the Rayleigh-Taylor instability which occurs during the acceleration phase of the target implosion. After a section in which the means to reach these goals will be reviewed, a second section will give one example of a 1D target design with emphasis on sensitivity studies. A following section will look at stability studies in 2D. Finally, a last section will conclude by summarizing and commenting on future developments.

II. ADVANTAGES OF QUARTER MICRON LASER LIGHT

The KrF has the shortest wavelength among lasers that have achieved more than a few kJ in the laboratory and is scalable to hundreds of kJ as shown in the FTF proposal. It has been shown to be operable at a high-repetition rate [7] and has achieved around 2000 continuous shots at 5

———————

*Electronic address: `Denis.Colombant@nrl.navy.mil`

Report Documentation Page

1. REPORT DATE **2007**	2. REPORT TYPE	3. DATES COVERED **00-00-2007 to 00-00-2007**

4. TITLE AND SUBTITLE **Direct-drive laser target designs for sub-MegaJoule energies**	5a. CONTRACT NUMBER
	5b. GRANT NUMBER
	5c. PROGRAM ELEMENT NUMBER
6. AUTHOR(S)	5d. PROJECT NUMBER
	5e. TASK NUMBER
	5f. WORK UNIT NUMBER

7. PERFORMING ORGANIZATION NAME(S) AND ADDRESS(ES) **Naval Research Laboratory,Plasma Physics Division,4555 Overlook Avenue SW,Washington,DC,20375**	8. PERFORMING ORGANIZATION REPORT NUMBER

9. SPONSORING/MONITORING AGENCY NAME(S) AND ADDRESS(ES)	10. SPONSOR/MONITOR'S ACRONYM(S)
	11. SPONSOR/MONITOR'S REPORT NUMBER(S)

12. DISTRIBUTION/AVAILABILITY STATEMENT
Approved for public release; distribution unlimited

13. SUPPLEMENTARY NOTES
This article appears in Physics of Plasmas and can be found at Colombant et al., Phys. Plasmas 14, 056317 (2007)

14. ABSTRACT

15. SUBJECT TERMS

16. SECURITY CLASSIFICATION OF:			17. LIMITATION OF ABSTRACT	18. NUMBER OF PAGES	19a. NAME OF RESPONSIBLE PERSON
a. REPORT **unclassified**	b. ABSTRACT **unclassified**	c. THIS PAGE **unclassified**	**Same as Report (SAR)**	**10**	

Hz, and 10^4 at 1 Hz. It also turns out that its short deep UV wavelength lends itself well to efficient target implosions. The first and most obvious advantage of the KrF wavelength is its high laser absorption efficiency. This has been known for a long time [3]. It has also been shown that the illumination uniformity in the focal spot can be achieved right out of the amplifier [8] and that its focal spot can be zoomed easily. Using zooming allows the focal spot size to be decreased in steps as the target implodes, which increases the coupling efficiency to the target.

A primary advantage of the KrF laser light for directly driven targets is that higher intensities can be utilized. This follows from the limit that is usually imposed on intensity due to the risks of generating fast electrons that can be detrimental to a successful core compression. These fast electrons are a by-product of laser plasma instabilities with thresholds scaling roughly as $I\lambda^2$, where I is the laser intensity and λ the laser wavelength. The KrF laser has an advantage of a factor of $(351/248)^2 = 2$ over 0.351 μm laser light. In other words, for the same $I\lambda^2$, the maximum intensity can be doubled for 0.248 μm light. The higher pressure achieved through higher laser intensity allows one to increase the velocity for a given aspect ratio or to lower the aspect ratio for a given velocity. There is usually a trade-off between implosion velocity and aspect ratio if the pressure is large enough. The higher implosion velocity can be desirable because it lowers the ignition energy whereas the lower initial aspect ratio provides more resistance to hydrodynamic instabilities. We have made the choice of increasing the velocity to values large enough for getting ignition energy at a sub-MJ level. The increase in implosion velocity also shows up in an improved hydrodynamic efficiency and this is another advantage of the shorter wavelength approach. Quantitatively, the maximum pressure achievable in spherical geometry has been shown to scale as $I^{7/9}\lambda^{-2/9}$ [4]. At constant $I\lambda^2$, the maximum pressure scales as P $(I\lambda^2)^{7/9}\lambda^{-16/9}$ or a factor of 1.85 advantage for the shorter wavelength compared to 0.351 μm light, from frequency tripled Nd-glass lasers.

Continuing with the constant $I\lambda^2$ argument, there are other advantages to the 0.248 μm wavelength. The main hydrodynamic instability occuring during acceleration of the target toward its stagnation stage is the Rayleigh-Taylor instability (RT) and the dispersion relation for this instability is given by the Bodner-Takabe formula [9, 10]

$$\gamma(t) = 0.9\sqrt{kg/(1 + kL_D)} - 3k(dm/dt)/\rho_{max} \qquad (1)$$

The stabilizing term is proportional to dm/dt, the mass ablation rate. That term scales as $I^{5/9}\lambda^{-4/9}$[4]. At constant $I\lambda^2$, it scales as $(I\lambda^2)^{5/9}\lambda^{-14/9}$. Compared to 351nm light, 0.248 μm laser light has a factor of 1.7 advantage. The ablative stabilization term is proportional to the mass ablation rate divided by the ablation density. For the target designs discussed here, we try to minimize ρ_{max} at the ablation surface and therefore we make use of
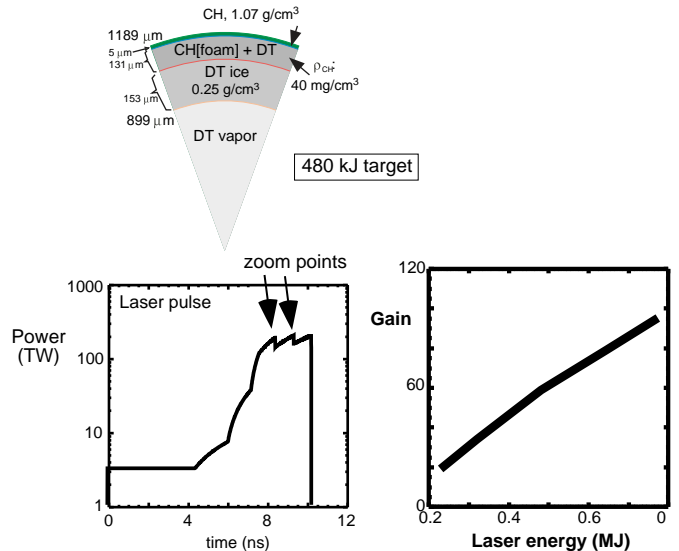

FIG. 1: Schematic diagram of a 500 kJ target with laser pulse history and plot of maximum implosion velocity vs. laser energy. The maximum intensity for this case is $2.5\times10^{15}W/cm^2$.

this beneficial scaling. The above scaling laws show that the shorter wavelength of the KrF laser is an advantage in many areas concerned with imploding targets.

III. EXAMPLE OF A 1D DESIGN AND SENSITIVITY STUDIES

Designs for sub-MJ targets have already been reported in references [6, 11]. Here we summarize the most important results and try to point out the differences between these designs and designs at higher laser energy (1MJ and above). First of all, Fig. 1 shows a typical target and laser pulse at 480 kJ. It consists of a CH overcoat (5 μm) on top of a Deuterium-Tritium(DT)-wicked foam ablator (130μm) and DT fuel (150μm). Although the fuel is thicker than the ablator, the ablator mass is larger by about 25% because of its larger mean radius. The aspect ratio for this target is 3.6. The pulse consists of a foot followed by a ramp up to the maximum power. There are no picket/spike prepulse used in this section of the paper although they will be included in the following section with 2D studies. The maximum implosion velocity for this target is 4.1×10^7 cm/s and the maximum intensity reached at the end of the laser pulse is $2.5\times10^{15}W/cm^2$. This type of target has been discussed at length in references [6, 11] and we present here sensitivity studies done on this design. The target dimensions given here and shown in the figure are those for the 480 kJ target and are scaled and optimized with laser energy in the gain-laser energy plot.

The sensitivity of the 480 kJ design to several parameters has been studied, including its sensitivity to laser intensity. Only one change at a time has been considered.
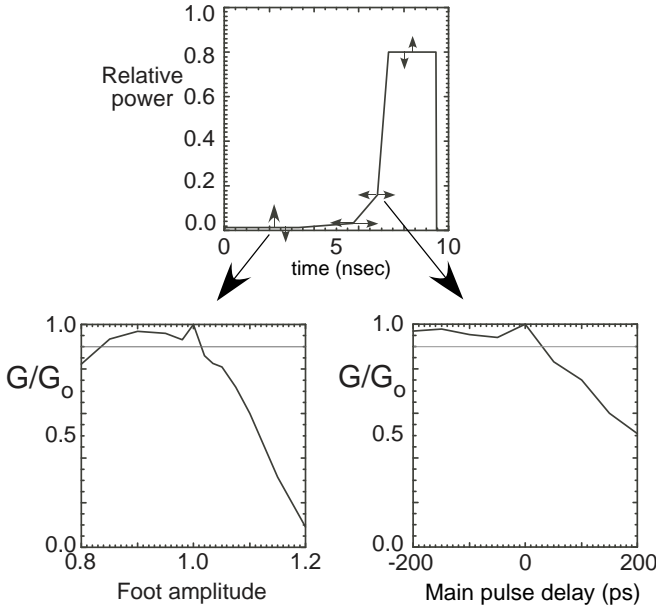
FIG. 2: Sensitivity plots for changes in the laser pulse shape. No spike is considered in this pulse. The figure shows changes in gain for variation in the foot amplitude and for variations in the timing of the last point in the rise of the main pulse (at 1/5 maximum power). The line at 0.9 of the normalized gain is a visual aid indicating 10% degradation in gain.
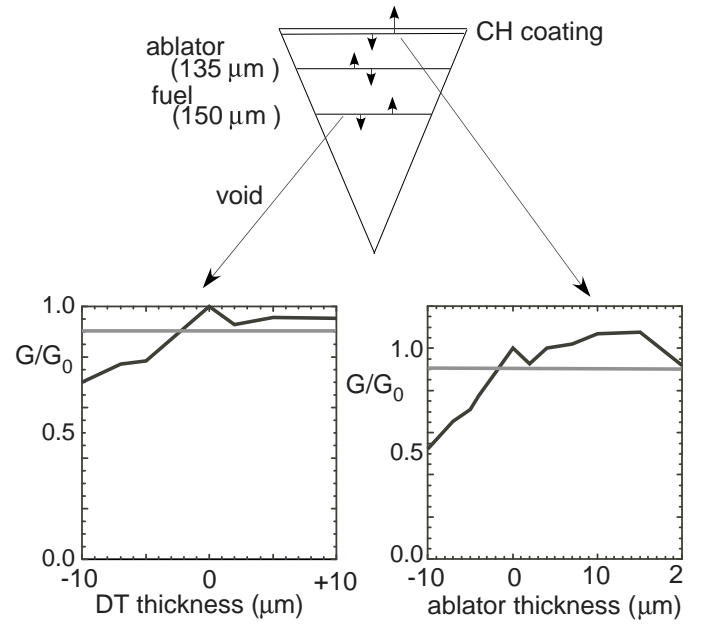

FIG. 3: Sensitivity plots for changes in the target shell thicknesses. The figure shows changes in gain for variations in the fuel thickness and in the ablator thickness. Note that an increase in the ablator thickness leads to slightly more gain than for the initial target.

This may represent a best case scenario since most likely, from shot to shot, imperfections will show up in several places at once, be it in the laser pulse or in the target dimensions. However, this allows us to identify the most critical areas of sensitivity, those which should lead to a tightened tolerance in the laser pulse shape or in the target dimensions specifications. The figure of merit used in this study is the gain.

Results for changes in the pulse are shown schematically in Fig. 2. The maximum power level is now flat which is slightly different from the pulse shape shown in Fig. 1 where the power showed a saw-tooth feature due to the zooming of the focal spot. In the pulse of Fig. 2, zooming still occurs but at constant power and it is the intensity on target (not shown) which now jumps slightly in time at the instant of zooming.

The flat-topped laser pulse qualitatively changes the maximum intensity in the target. In the previous design, the power peaks at the end of the laser pulse when the mean absorption radius is smallest. These two factors (maximum power, smallest radius) make the intensity strongly peaked at the end. In the flat-topped pulse, the intensity does not peak so strongly, but remains high for a longer period of time. This has implications when considering the effects of hot electron preheat that are strongly driven by the laser intensity. The change resulting from the pulse reconfiguration is not very large since the maximum intensity decreased from 2.5 to $2.3 \times 10^{15} W/cm^2$ between these two cases.

Many changes have been considered in the laser pulse

shape. We varied the rate in the rise of the foot, the length of the foot, the time delays (positive or negative compared to the original pulse shape) of the various points in the ramping up of the main pulse, the final level of the main pulse and the amplitude of the foot. Changing the final level of the main pulse changed the energy delivered to the target and increased (or decreased) the laser intensity. The most critical parameters have been found to be the amplitude of the foot and the rate of rise of the pulse in its final stage. While these changes were made, the timing of the shocks was affected. Because the original timing was off, the gain decreased from its optimum value. The first critical change shown in Fig. 2 occurs for the foot amplitude. Changes in gain are minor when the foot amplitude is decreased but a larger gain deterioration occurs for a higher foot amplitude than the original one. This is simply because the foot amplitude sets the adiabat of the target and an increase in foot amplitude increases the adiabat of the fuel. An increase in foot amplitude of 5% will bring a decrease in gain of 22%, so the foot level has to be controlled quite accurately in order to avoid this degradation. The other critical parameter in the pulse shape is the rate of rise of the last stage in the main pulse. The figure shows that when the time of the last point (20% of maximum power) is advanced, little change occurs in the gain. However, when the time is delayed the gain drops significantly. This can be explained by the launching of a strong late shock through the target, again increasing the adiabat and degrading the gain.

The second set of changes involved the target dimensions as shown in Fig. 3. Successively, the various shell thicknesses (CH overcoat, ablator, fuel) have been modified. Also, but not shown in Fig. 3, interchange between fuel and foam has been considered. Again, every change in thickness of the target, be it in the fuel or the ablator, leads to a change in shock timing and results in a drop from the maximum gain. The figure shows that an increase in fuel or ablator thickness results in a minor change in the gain whereas a decrease in the same quantities shows a more noticeable drop. When there is a decrease in any shell thickness, the fuel mass is decreased (in the case of a thinner ablator, more fuel is ablated before the start of the burn). Another (unexpected) result is that an increase in the ablator has increased the gain. This shows that the target was not quite optimized although the new maximum gain is only 7.5% higher. In summary of these sensitivity studies, the pulse is most sensitive to the amplitude of the foot and to the rate of rise of the last stage of the main pulse. As for the target, decreasing the thickness of the layers by a few % can lead to a signficant loss of gain.

IV. STABILITY AND GAIN STUDIES IN 2D

For stability studies, additional designs were considered including a picket/spike prepulse. These spikes provide the means for adiabat shaping [16] and thus help contribute to the overall performance of targets. They have also been shown to reduce Richtmeyer-Meshkov (RM) instabilities by modifying the density profiles during the initial interaction of the laser pulse with the target [13]. The general idea behind the use of spikes is simpler to visualize for the relaxation type which is going to be described shortly. The idea is to send a decaying shock into the target with a rarefaction wave decompressing the ablator. When the foot of the pulse turns on, another shock is launched up the rarefaction wave, heating the outer portion of the target more. The result is a shaped adiabat higher on the outside than on the inside. Perturbations on the shock decay faster as they travel up the density gradient, so imprint is also mitigated. In all the designs considered here, the shock from the spike and the shock from the foot pulse almost catch each other as they break-out from the rear of the fuel shell. The degree of adiabat shaping is determined by the amplitude and width of the spike (energy in the spike) or by the intensity of the foot pulse.

Two classes of spike prepulse designs were used that give varying degrees of adiabat shaping. In the first class called relaxation type (RX)[14], the laser power turns off at the end of the spike. After a small amount of time, the pulse is turned on again, driving a shock up the rarefaction wave. These pulses are shown in Fig. 4. In all these pulses the spike intensity was 65 TW/cm^2 and had a 200 ps full width at half-maximum. The main difference between the designs was primarily the amplitude of the
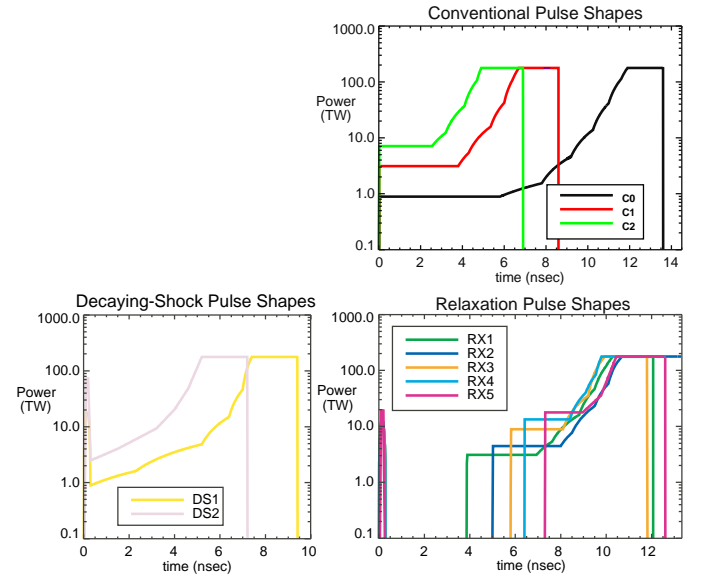

FIG. 4: (Color) Various pulse shapes for 2D runs. They show conventional, relaxation type spike and decaying shock spike pulse shapes. Besides the presence of a spike prepulse, the main difference between these different pulse shapes is the amplitude of the foot intensity which controls the final adiabat of the implosion.

foot, which varied from 17 to 100 TW/cm^2. In the second class of spike prepulse designs, called decaying shock (DS)[15], the power level after the spike merges immediately into the foot pulse. There is no delay as with the RX pulse. The primary ablator preheat mechanism in the DX pulse is shock-heating by the spike, rather than the expansion followed by shock heating of the RX pulse. These pulses, also shown in Fig. 4, have a spike that is typically larger than in the previous RX pulses. Finally, the conventional pulses are similar to the case shown in the previous section where the foot amplitude has been changed. The target remains the same as in the previous section except that the CH overcoat was removed to simplify the simulations. 1D results for these different pulse shapes are shown in table I.

The table shows that the C2 target has approximately the same foot amplitude as target RX3. These two targets are similar in terms of stability (in-flight aspect ratio [IFAR], number of e-folds), but have quite different gains, 20 for C2 and 63 for RX3. This correlates with their differences in fuel α at the time before burn, 7.3 for C2 and 4.6 for RX3 where α is the ratio of the total pressure to the Fermi-degenerate pressure and is also referred to as the adiabat. The locally varying α's in these various targets are shown in Fig. 5 as a function of normalized mass at the time when 1/2 of the total initial mass has been ablated. The adiabat at the ablation surface (where there is a sharp upturn) varies from case to case. The highest adiabats at the ablation fronts (yielding the higher stabilization) occur for the RX pulses whereas the adiabats for the conventional pulses are almost completely

TABLE I: Parameters for the 500 kJ target with different pulse shapes. C stands for conventional, RX for relaxation prepulse and DS for decaying shock prepulse. The numbers after the pulse descriptors increase with increasing foot intensity within the same pulse group. IFAR, the in-flight aspect-ratio, is defined at 2/3 of the original target radius. The adiabat, α, is the ratio of the fuel pressure to the Fermi-degenerate pressure, mass-averaged in the region between 1/e of the maximum density, just before the time of ignition. The margin is defined as the fractional remaining kinetic energy when gain=1. The "Foot" is the ratio of the foot power to the main pulse power, except for the DS pulses where it is defined as the ratio of the spike energy to the main pulse energy.

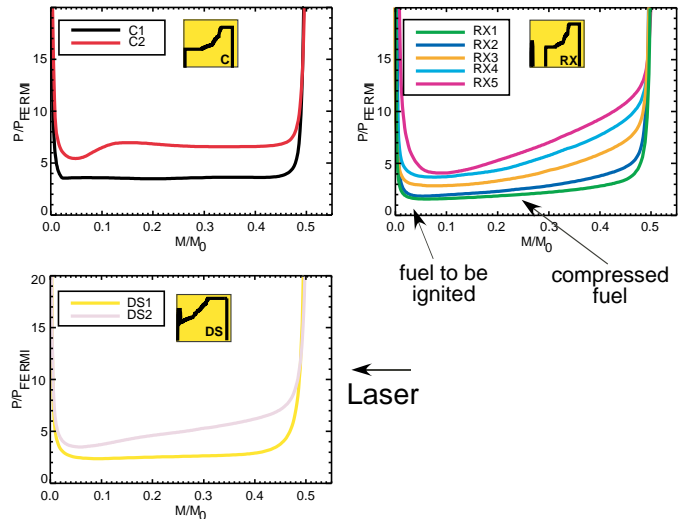| Pulse	Gain	Max efolds	IFAR	α	ρR_{max}	margin	Foot
C0	99	8.8	49	2.3	1.88	0.44	0.05
C1	66	5.6	33	4.5	1.50	0.44	1.75
C2	20	3.7	21	7.3	1.18	0.31	4.0
RX1	79	6.2	36	3.0	1.63	0.38	1.75
RX2	75	5.4	30	3.4	1.64	0.44	2.5
RX3	63	4.5	26	4.6	1.55	0.43	5.0
RX4	49	3.8	22	5.9	1.39	0.34	7.5
RX5	16	3.4	19	6.8	1.18	0.21	10.0
DS1	69	5.7	36	3.5	1.47	0.33	0.8
DS2	49	3.7	22	5.6	1.38	0.36	2.2

FIG. 5: (Color) Fuel adiabats for the various pulses when 50% of the mass of the target has been ablated. The conventional pulses show no gradient in the adiabat whereas the spike pulses show the presence of a gradient in these curves. The ablation surface is where the adiabat turns upward sharply. The laser light comes from the right of the figure and the fuel to be ignited lies near the center of the target.

flat. Because of the higher adiabat at the ablation front, a gradient in the adiabat appears which determines the adiabat shaping and which leads to a stronger stabilization of the targets. However, the adiabat near the center ($m/m_0 \rightarrow 0$) also indicates how strong the compression will be and is predictive of the gain. For example, we can see that the pulse RX5, which has a gain of only 16, has a larger adiabat in the innermost part of the fuel.

The various designs were next simulated in 2D ($r - \theta$ geometry) and included initial areal mass perturbations of the outer surface finish. The 2D FAST code [21] used for the calculations makes use of a low noise algorithm for hydrodynamics [22], laser ray-tracing and deposition, radiation transport and electron and ion thermal diffusion. These simulations use 45 photon energy groups. They are run in a conservative mode (solving the conservation equations for total energy instead of evolution equations for internal energy) in order to insure the proper shock heating and consequently their correct speed of propagation. A harmonic flux-limiter was used for thermal transport with a standard value of 0.1.

We initially concentrate on outer surface perturbations since they grow both early and quickly. Earlier design studies [17] have shown outer perturbations to be of primary importance. The initially larger inner surface perturbations do not grow until after the initial compression phase. Imprint may be important but can be mitigated by thin high-Z layers as shown by experiment[18]. We leave consideration of these and other sources of nonuni-

formity for future studies.

We make heavy use of high-resolution simulations that encompass a large range of perturbation wavelengths. Such simulations in the linear regime are useful to study the relative importance of the different modes and their growth factors. In the nonlinear growth regime, these simulations will give realistic mode-mode coupling and saturation, as well as their effect on gain. These high-resolution simulations use 660 points in the radial direction and 2048 points in the azimuthal direction over a quarter sphere, running from a pole to the equator. All even modes from $l = 2 - 512$ are resolved (a mode is considered resolved when it is described by 16 points per wavelength). We measure perturbations by integrating the density from the inside outward to define an areal mass, $\int \rho dr$. This measure includes perturbations throughout the target, even if they do not lie entirely on the ablation surface.

We begin with simulations that use very small initial amplitude perturbations (1 nm total σ_{rms}) to validate growth in the linear regime. These perturbations are extremely tiny to ensure that they remain in the linear regime during their subsequent growth. We expect primarily RM growth during the initial compression phase of the target, before the initial shocks have reached the inside edge of the solid fuel shell ("shock break-out"). After this time, the pellet is accelerated by the laser pulse and RT growth occurs. Fig. 6 shows results for the conventional pulses C1 and C2. It shows the growth factor at the times of the shock break-out and peak velocity. The growth factor is defined by comparing the areal-mass amplitude of each mode at the chosen time to its initial

Linear Growth Factor

$$\frac{\Delta\rho R(t)\,\rho R_0}{\rho R(t)\,\Delta\rho R_0}$$

C1

RM (breakout)
RM+RT (V_{max})

ℓ

Linear Growth Factor

$$\frac{\Delta\rho R(t)\,\rho R_0}{\rho R(t)\,\Delta\rho R_0}$$

C2

RM (breakout)
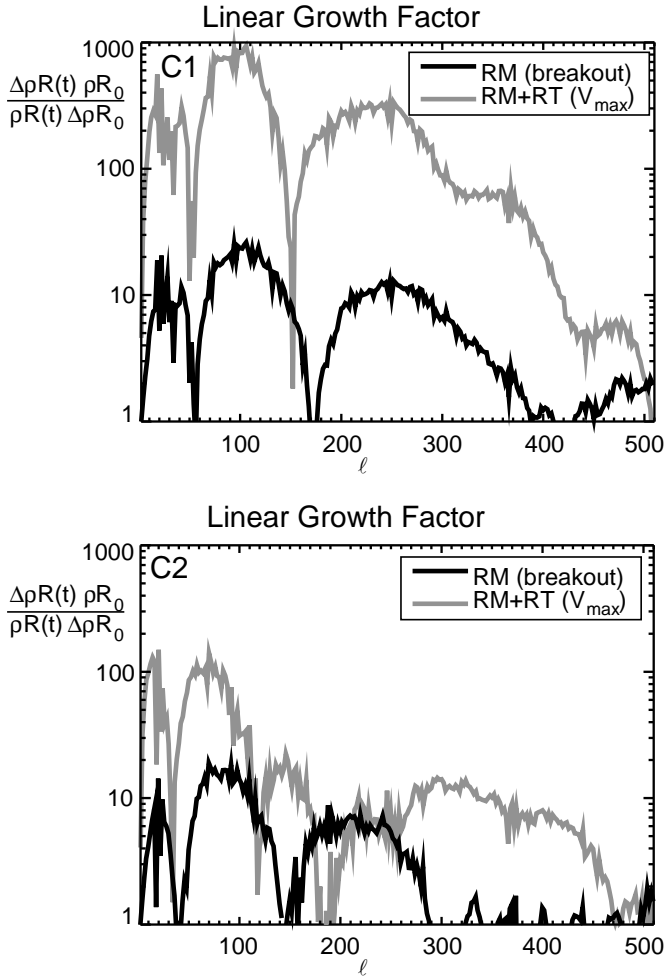RM+RT (V_{max})

ℓ

FIG. 6: Growth factors from a 2D computation for conventional pulses C1 and C2 (different foot strength). The plots show the growth after shock break-out (RM only) and at peak velocity (both RM and RT are included).

(t=0) amplitude. As the growth at peak velocity includes both the RM and the RT growths, it is expected to be larger than the earlier 1D estimates that only include RT growth. The results show that RM growth is of the order of ten and total growth of the order of 3 orders of magnitude for C1 and just above 2 orders of magnitude for C2. In terms of number of e-folds, it is around 7 for C1 and around 5 for C2. If we substract the maximum growth for RM at these very same modes, we obtain 4 e-folds for RT for C1 and 2 for C2. These numbers are smaller than the maximum number of e-folds shown in table I, which include RT only and are based on spatial amplitude growth, not areal mass.

Next, we turn our attention to perturbations that are considered realistic, and that can develop nonlinearly. An acheivable pellet surface finish has a total rms value of about $1/8$ μm rms in CH, and exhibits a NIF (National Ignition Facility)-like standard spectrum [19], modified at the lowest l-modes [20]($l < 4$). Fig. 7 shows results

$$\left(\Delta\rho R(t)/\Delta\rho R_0\right)\left(\rho R_0/\rho R(t)\right)$$

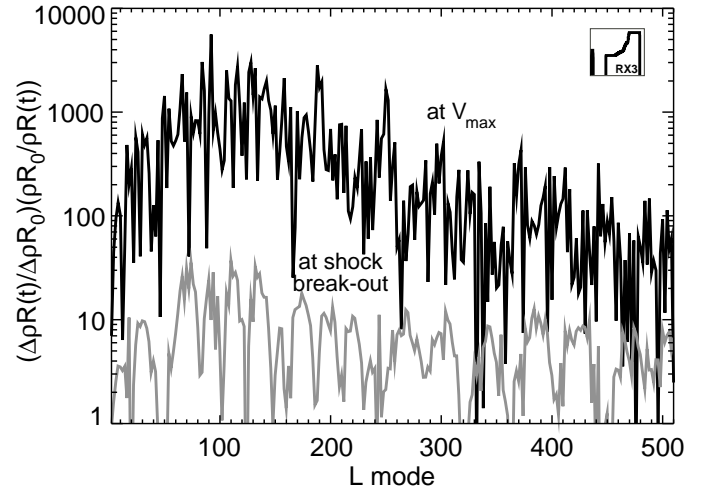at V_{max}

at shock break-out

L mode

RX3

FIG. 7: Growth factor from a 2D computation for pulse RX3. Plot shows growth after shock break-out and at peak velocity. Initial outer surface perturbations are realistic ($1/2$ μm rms). Note that the maximum growth factor is around 10^3. Density images from this simulation are shown in Fig. 9.

mode amplitude vs. time

Normalized Mode amplitude (g/cm^2)

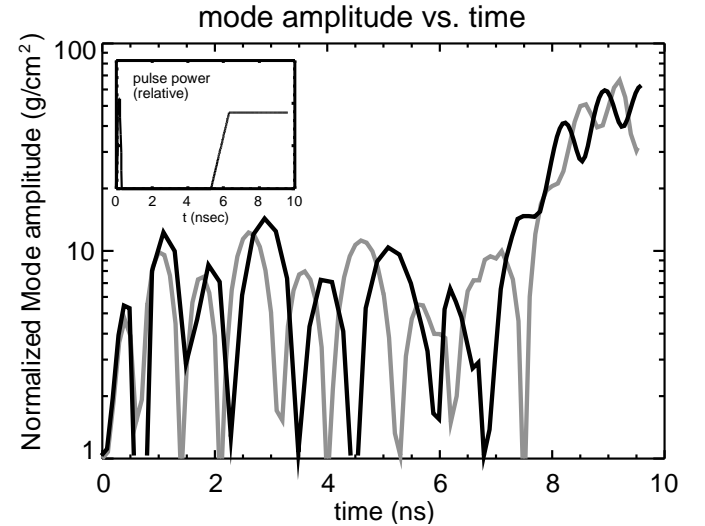pulse power (relative)

t (nsec)

time (ns)

FIG. 8: The growth of mode $l = 176$ in the RM stage for RX3 pulse, for the FAST code (black lines) and a linear spectral code (gray lines). The inset shows the pulse power.

of a pellet implosion with this initial perturbation level. In that case, the pellet was driven by the RX3 pulse. Since the CH outer layer was neglected, the actual surface finish was about $1/2$ μm rms in the CH/DT foam. The maximum growth for RM is about 20-30 and slightly above 10^3 for RM + RT. The corresponding number of e-folds is 3 for RM and 7 for total growth. If we subtract the RM growth, this becomes around 4 for RT which is slightly less than the number shown in table I for the maximum number of e-folds. The most significant result is the gain of 57 achieved for this case which reaches 90% of the clean 1D yield (63). This result shows that the goal laid out in the introduction may be possible.
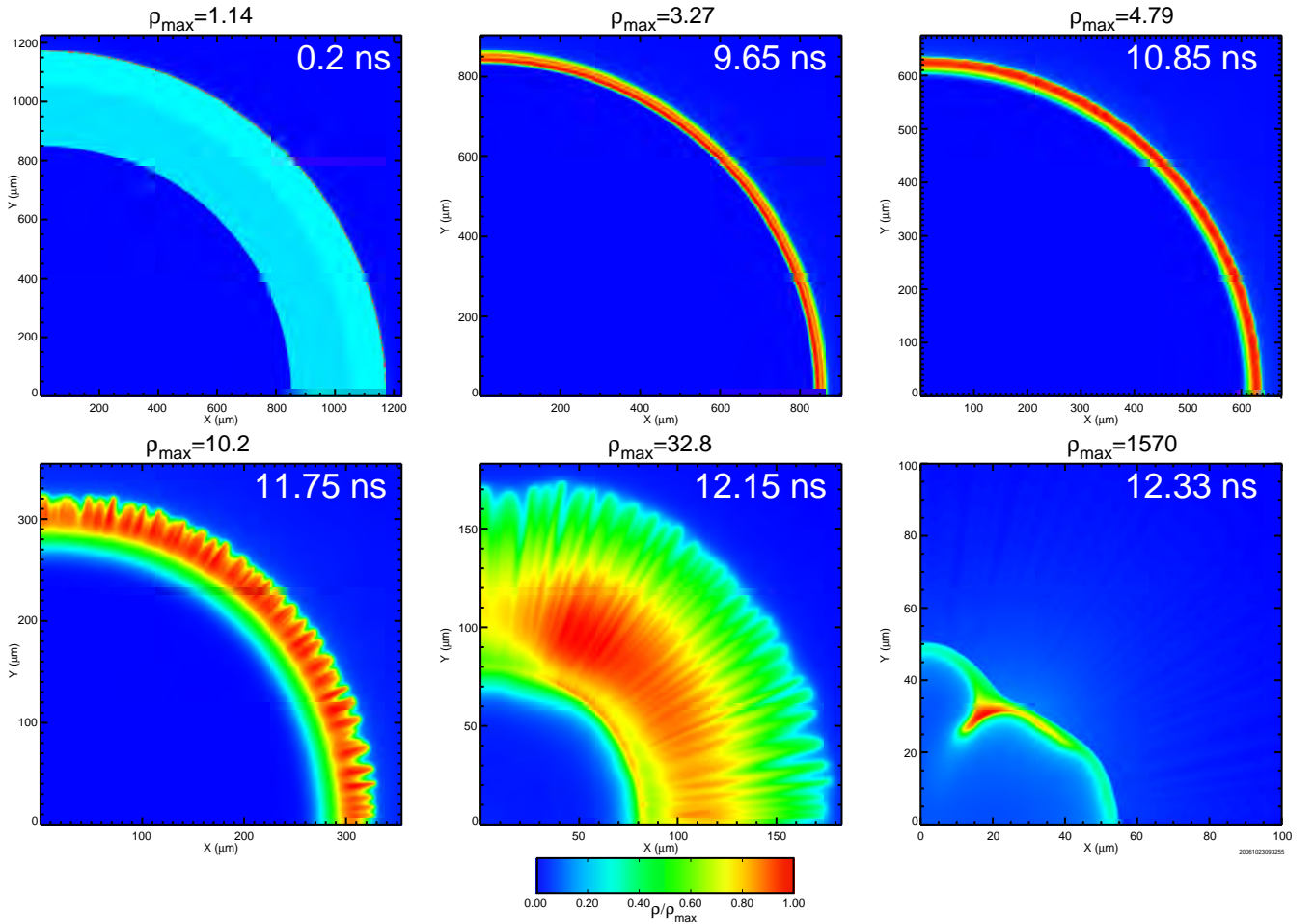
FIG. 9: (Color) Density images of the RX3 500 kJ target at different times during implosion. This case has a yield over clean 1D yield ratio of 0.9.

Before going any further, a few words need to be said about the computational requirements for obtaining an accurate solution in the case of spike pulse shapes, especially of the RX type. Early in time during the compression stage, the shock launched by the spike propagates into the target while a rarefaction wave blows off the plasma. When the shock due to the foot of the main pulse is launched, a new ablation front appears away from the first shock and the separation between the first shock and the former ablation front can reach a few hundred microns. However, the solution requires high resolution in the vicinity of this second front (of the order of a μm) while simultaneously resolving the former ablation surface to order 0.1 μm. Failure to keep adequate resolution in both places simultaneously gives an inaccurate solution and perturbation growth that is anomalously high. This was checked with the full 2D code, and also cross-checked with a linear spectral code [22]. The linear spectral code contains only the essential physics (hydrodyamics, electron thermal conduction, ideal equation-of-state, and laser absorption) and can only run a single mode at a time; however, it has more accurate hydrodynamics, and

can use an order of magnitude more axial points for high resolution (0.1 μm) everywhere. Results from this code and FAST are shown in Fig. 8 for mode $l = 176$ which is among the fastest growing modes as shown in Fig. 7. We used the results of this comparison to constrain the gridding used in the FAST simulations presented here. This is an example of our use of a multicode approach in target design in order to validate and check on the FAST code results.

Fig. 9 shows density images at several times during the implosion of the RX3 target on its way to implosion and burn. The most noticeable feature of these plots is that the small wavelength perturbations (high l modes) do not tear the target apart as can be seen sometimes in unsuccessful implosion runs. (As one example [not shown here], the C0 pulse produces so much growth of high mode perturbations in the pellet that the fuel shell is completely shredded before ignition, and the pellet fails to ignite.) This target is thus quite robust to RT instabilities and that is one reason behind the very good yield. Another noticeable new feature, is the dominance of a low $l = 4$ mode during burn in the last frame.
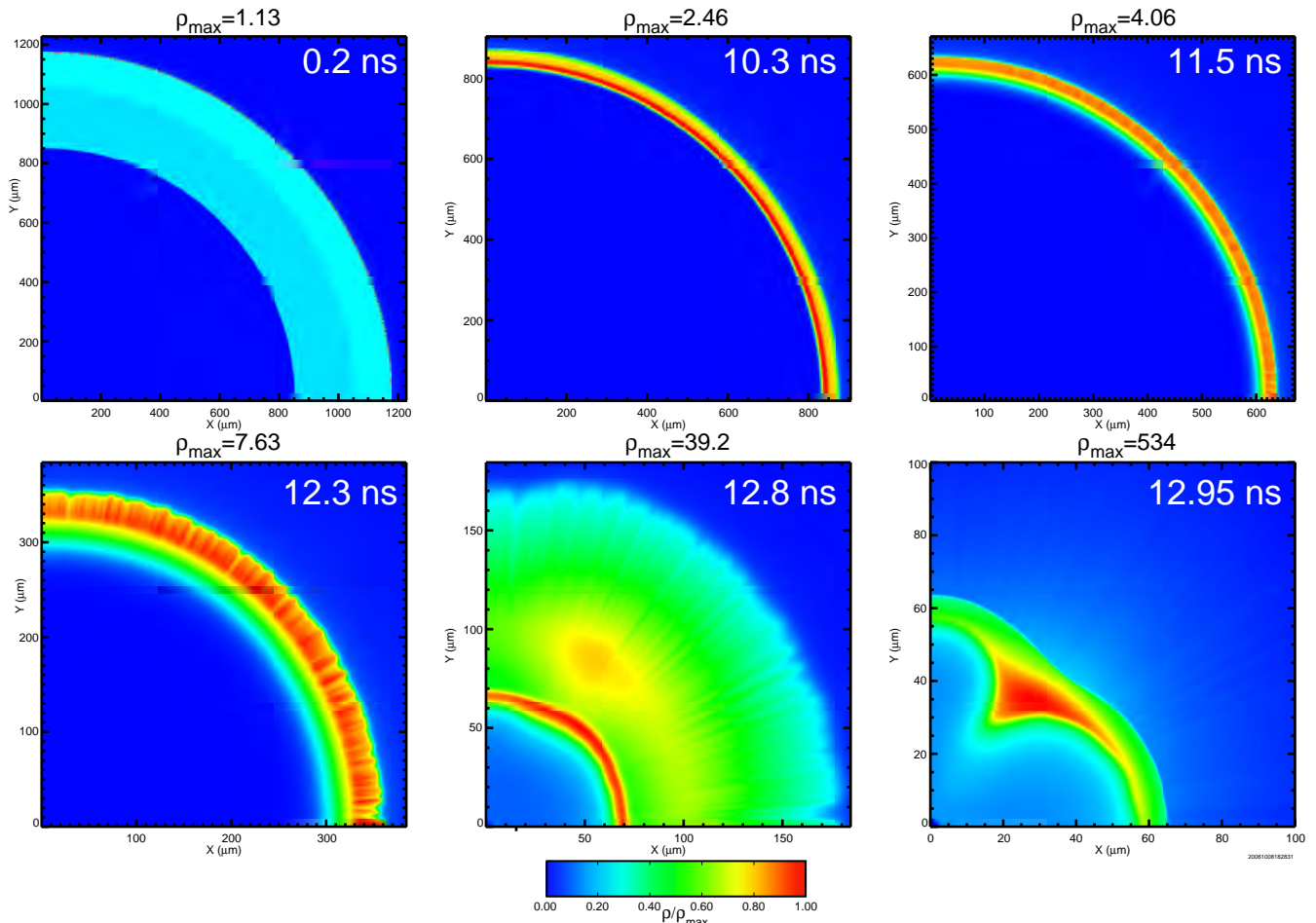
FIG. 10: (Color) Same plot as Fig. 9, but for the RX5 pulse. The ratio of yield over clean 1D yield is 0.05.

In Fig. 10 we show a similar plot for the case RX5 which is not as successful as RX3. The RX5 pulse has a higher foot than RX3 and as a consequence is more stable to RT growth at large l mode. In spite of the increased stability at high mode numbers, the yield is only 5% of 1D. However, the general features for this run are qualitatively similar to those of the previous case and, in particular at burn time, the same low mode $l = 4$ behavior dominates.

This increased sensitivity to low l-mode disruption of the gain is a general feature seen in these higher adiabat targets. To show this, we have performed a set of low-mode-only simulations, using the same designs and configurations but including only 64 points equally spaced in the azimuthal direction. This will give accurate resolution of low modes $l = 2 - 16$ and predicts the sensitivity of the pellets to just these low modes. (The NIF-standard spectrum used in these calculations contains the bulk of its nonuniformity in the very lowest modes $l < 10$). Fig. 11 shows a plot of the yield over 1D yield as a function of the mass-averaged α for various pulse shapes. All pulses show a deterioration of the gain with increasing α. This feature deterioration is correlated with the igni-

tion delay time shown in the adjacent plot. (The ignition delay time is defined as the time between the maximum ρR and the time of half-maximum yield). The higher adiabat targets take more time to begin to burn after maximum compression. This makes them more sensitive to low-mode perturbations that can reduce the conversion of the stagnating fuel kinetic energy into the internal energy of the igniting spark plug.

V. CONCLUSIONS

Our simulations show that gains larger than 50 are feasible with 500 kJ, 0.248 micron laser light, and that the targets appear to be robust against Rayleigh-Taylor instabilities. This is a significant step toward the goal laid out by the FTF proposed at NRL. These designs make use of early-time spikes in the pulse shape to achieve tailored adiabat. The simulations also show that yields in higher adiabat (more RT stabilized) designs are more sensitive than lower adiabat designs to low l mode growth during fuel shell deceleration and ignition.

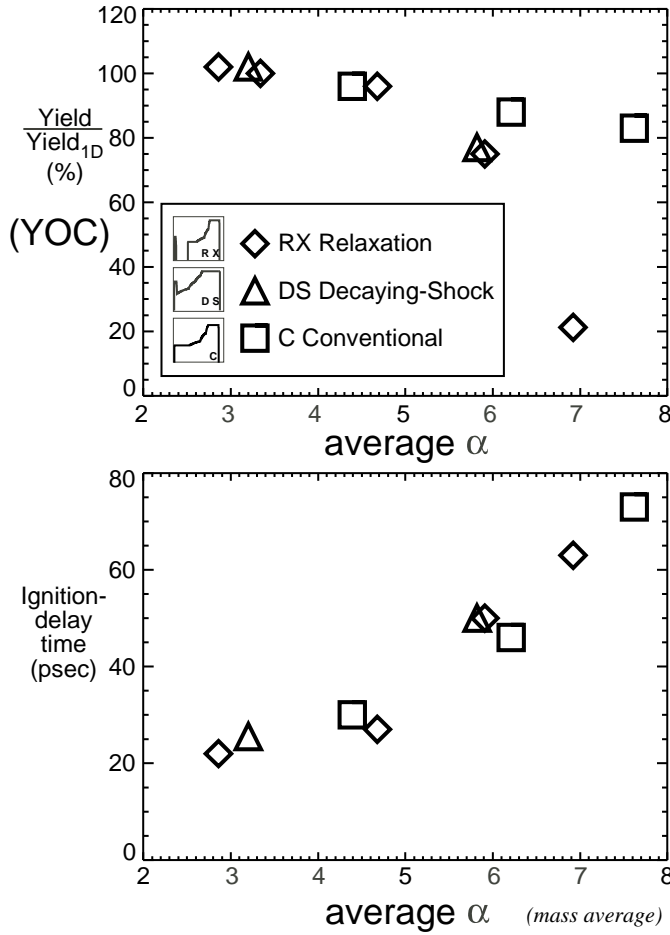These initial simulations focused on growth of outer

FIG. 11: (a) Yield over 1D yield as a function of adiabat for RX, DS and conventional pulses. (b) The time delay between maximum compression (ρR) and half-maximum fusion yield as a function of adiabat.

surface perturbation, as previous results have shown that inner fuel surface perturbations do not seem to be as damaging as outer perturbations[17]. However, other sources of seeds for the Rayleigh-Taylor instability need further examination before firm conclusions are made. For imprint reduction, the possibility exists of using a high-Z layer as proposed and demonstrated in earlier work[18]. More physics can be added to these computations like a better nonlocal electron transport which remains one of the challenging problems in laser-matter interaction. Finally, the approximate value of the threshold or destructive intensities for laser plasma instabilities (particularly two-plasmon decay) remains unknown. More experiments are needed in this area, particularly at KrF's 248 nm wavelength, to make progress on this issue.

[1] J. Nuckolls, L. Wood, A. Thiessen and G. Zimmerman, Nature, **239**, 139 (1972).

[2] S. Atzeni and J. Meyer-ter-Vehn, *The Physics of Inertial Fusion*, Oxford Science Publications, 2004. pp. 107, 109, 117.

[3] Ibid., p. 380.

[4] Ibid., p. 212.

[5] S.P. Obenschain, S.E. Bodner, D.G. Colombant *et al*, Phys. Plasmas **3**, 2098 (1996).

[6] S. P. Obenschain, D. G. Colombant, A. J. Schmitt *et al*, Phys. Plasmas **13**, 056320 (2006).

[7] J. Sethian, M. Friedman, J. Giulani *et al*, Phys. Plasmas **10**, 2142 (2003).

[8] R.H. Lehmberg and J. Goldhar, Fusion Tech. **11**, 532 (1987).

[9] S.E. Bodner, Phys. Rev. Lett. **33**, 761 (1974).

[10] H. Takabe, R.L. Morse *et al*, Phys. Fluids **28**, 3676 (1985).

[11] D.G. Colombant and S.P. Obenschain, Nucl. Fusion **47**, 17 (2007).

[12] W. Levedahl and J .Lindl, Nucl. Fusion **37**, 165 (1997).

[13] N. Metzler, A.L. Velikovich and J.H. Gardner, Phys. Plasmas **6**, 3283 (1999).

[14] K. Anderson and R. Betti, Phys. Plasmas **11**, 5 (2004).

[15] V.N. Goncharov, J.P. Knauer, P.W .McKenty *et al*, Phys. Plasmas **10**, 1906 (2003).

[16] S. E. Bodner, D. G. Colombant, J. H. Gardner *et al*, Phys. Plasmas **5**, 1901 (1998).

[17] A. J. Schmitt, D. G. Colombant, A. L. Velikovich *et al*, Phys. Plasmas **11**, 2716 (2004).

[18] S. P. Obenschain, D. G. Colombant, M. Karasik *et al*, Phys. Plasmas **9**, 2234 (2002).

[19] A.I. Nikitenko, S.M. Tolokonnikov, and R. Cook, Fusion Tech. **31**, 385 (1997); R.C. Cook, R.L. McEachern, and R.B. Stephens, Fusion Tech. **35**, 224 (1999).

[20] A .Nikroo, J.Bousquet, R.Cook *et al*, Fusion Sci. Tech. **45**, 165 (2004).

[21] J. H. Gardner. A. J. Schmitt, J. P. Dahlburg, *et al*, Phys. Plasmas **5**, 1935 (1998).

[22] S. T. Zalesak, A. J. Schmitt, A. L. Velikovich and J. H. Gardner, Phys. Plasmas **12**, 056311 (2005).